Simplified prediction models for acoustic installation effects of train-mounted equipment

David Thompson, ORCID: 0000-0002-7964-5906

Institute of Sound and Vibration Research, University of Southampton, Southampton SO17 1BJ, UK

Corresponding author, email: djt@isvr.soton.ac.uk

Dong Zhao, ORCID: 0000-0002-1380-9306

Institute of Sound and Vibration Research, University of Southampton, Southampton SO17 1BJ, UK

Giacomo Squicciarini, ORCID: 0000-0003-2437-6398

Institute of Sound and Vibration Research, University of Southampton, Southampton SO17 1BJ, UK

Abstract

Acoustic models of railway vehicles in standstill and pass-by conditions can be used as part of a virtual certification process for new trains. For each piece of auxiliary equipment, the sound power measured on a test bench is combined with measured or predicted transfer functions. It is important, however, to allow for installation effects due to shielding by fairings or the train body. In the current work, fast-running analytical models are developed to determine these installation effects. The model for roof-mounted sources takes account of diffraction at the corner of the train body or fairing, using a barrier model. For equipment mounted under the train, the acoustic propagation from the sides of the source is based on free-field Green's functions. The bottom surfaces are assumed to radiate initially into a cavity under the train, which is modelled with a simple diffuse field approach. The sound emitted from the gaps at the side of the cavity is then assumed to propagate to the receivers according to free-field Green's functions. Results show good agreement with a 2.5D boundary element model and with measurements. Modelling uncertainty and parametric uncertainty are evaluated. The largest variability occurs due to the height and impedance of the ground,

especially for a low receiver. This leads to standard deviations of up to 4 dB at low frequencies. For the roof-mounted sources, uncertainty over the location of the corner used in the equivalent barrier model can also lead to large standard deviations.

Keywords: Train noise; Auxiliary equipment; Acoustic installation effects; Virtual certification; Uncertainty

Statements and Declarations

1. Introduction

Railways in many countries have seen considerable expansion in recent decades in terms of both new lines and increased traffic operating on their networks. Although railways offer an environmentally friendly transport option, the noise produced is a major source of disturbance for nearby residents. An important strategy that is adopted to control railway noise is to specify limit values for the noise emission of new trains. In Europe, such noise limits are defined for new and refurbished rolling stock in the Technical Specification for Interoperability (TSI) for noise [1]. The limits apply to standstill, pass-by and starting conditions, based on measurements according to ISO 3095 [2]. Due to the expense of these measurements, and the difficulty to find and maintain suitable test sites, the concept of virtual testing and certification provides an attractive alternative.

Virtual testing based on computational models is widely used, for example in the automotive field, including for crash testing [3], fatigue assessment [4], and durability [5]. Hybrid approaches combining virtual testing with laboratory test rigs are also being introduced [6]. In the railway field, virtual testing has been introduced for rail vehicle dynamics [7, 8], train aerodynamics [9, 10] and pantograph-catenary interaction [11]. They are also reflected in the revision of the relevant European standards.

The EU project Acoutrain (2011-2014) had the goal of simplifying and improving the acoustic certification process of new rolling stock, principally through proposing virtual testing concepts for acoustics [12]. The virtual testing procedure relies on a global modelling approach for the noise from the rolling stock, in which each item of equipment on the train, as well as rolling noise sources, are defined in terms of their sound powers and transmission paths. In Acoutrain, such a global model of a vehicle was called a virtual vehicle [12, 13]. Typically, in a so-called extension of approval process [12], a virtual vehicle model would be generated for one train type and validated using measurements. Variants that are derived from this train type but, for example, contain alternatives to some items of equipment, could then be certified by updating the virtual vehicle model using source data from the alternative equipment.

This modelling approach for a virtual vehicle is implemented in various in-house software tools that are used within the railway industry [14, 15]. In addition, within the Acoutrain

project a dedicated global prediction tool was developed that contained the basic calculations required for a virtual vehicle model [16]. Sources may be defined as point sources, area sources or box sources.

Source strengths of equipment are typically measured on a test bench in the form of sound powers. These may be sub-divided into the power radiated by each face of a box source, obtained using sound intensity scanning [17]. Alternatively, basic directivity information may be obtained from free-field sound pressure measurements used to determine the source sound power [18].

This source information is typically entered into the virtual vehicle model in one-third octave bands [14, 15, 19]. The sound transmission from each source to the standard receiver positions is then calculated, using free-field propagation and also allowing for ground reflections. The effect of source motion can also be taken into account, including the Doppler effect [16]. However, the situation is complicated by the presence of elements on the train that provide shielding, such as skirts and screens and the train body itself. Depending on the simulation tool to be used, two main options were identified in the Acoutrain project for dealing with these installation effects [13]:

1. Define a source model that accounts for the installation effects through an apparent directivity.
2. Define a source model that does not account for the installation effects. Then the tool must be able to calculate the installation effect.

Although some of the in-house tools contained simple screen models, the Acoutrain global modelling tool was based on the assumption that the installation effects would be provided as part of the source model, for example as modified directivities [16]. In practice, however, this data is not typically available.

Validation of the virtual vehicle approach was carried out in the Acoutrain project on a train called the NAT [13]. A key issue identified was that, due to the installation effects of sources such as the heating, ventilation and air conditioning (HVAC) system and the traction motor cooling unit, the overall standstill noise was overestimated by an average of 3-4 dB(A), and by more than this for some individual microphone positions.

The aim of this paper is to propose simple models to allow for installation effects and to validate them by comparison with more complex numerical models and with measurements. The main installation effect is due to shielding by fairings, screens or by the train body itself. In addition, there may be changes to the sound emission of the source, for example due to changes in the loading of fans. However, these are neglected in the current work. A distinction is made between equipment mounted on the roof, considered in Section 2, for which a classical diffraction model is proposed, and equipment mounted under the train, for which a model of a semi-reverberant field is introduced in Section 3. In each case a numerical model is established using the 2.5D boundary element (BE) method [20], which is used as a reference for comparison with the proposed analytical models. Comparisons are also made with measurements for the underframe-mounted source. Finally, in Section 4, an assessment is made of sources of uncertainty.

2. Roof-mounted sources

In this section the sound radiation from a source mounted on the train roof is first assessed by using a 2.5D BE approach for different train geometries. An analytical approach is then introduced, based on Pierce's formulation for diffraction of sound around a barrier [21, 22]. A similar approach was also considered by Orrenius et al. [19] and showed good agreement with measurements for simple source-receiver geometries.

2.1 Models

2.1.1 Selected train geometries

Four generic train geometries are considered, to represent typical train roof profiles, as shown in Fig. 1. These are (a) a roof with rectangular corners, (b) a roof with chamfered corners, (c) one with rounded corners and (d) one with fairings. Only a single fairing is considered in Fig. 1(d) as it was found that, otherwise, the results are affected by strong reflections between the two fairings. In reality, these reflections would be disturbed by the equipment mounted between the two fairings, the details of which are not considered here. In each model, the train roof is set to be 4 m above the ground and the train floor is 0.75 m above the ground. The width of the train body is 2.5 m for the model in Fig. 1(a) and 2.9 m for the models in Fig. 1(b-d).
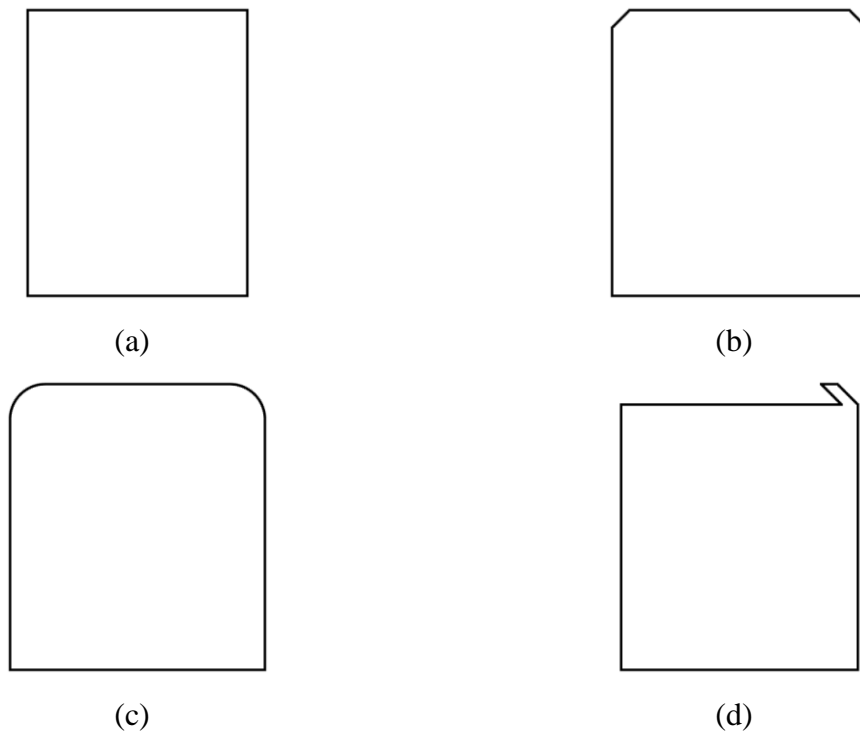
Fig. 1 Four train geometries used in 2D BE models. (a) Rectangular train geometry; (b) train roof with chamfered corners; (c) train roof with rounded corners; (d) train roof with single fairing

Fig. 2 shows the positions of the sound source and the receivers. The source is assumed to be embedded at the centre of the roof and the receivers are placed at 7.5 m away from the train centreline. The height of these receivers extends from 5 m below the ground level (to account for ground reflections) to 9 m above the ground level, with a spacing of 0.5 m.
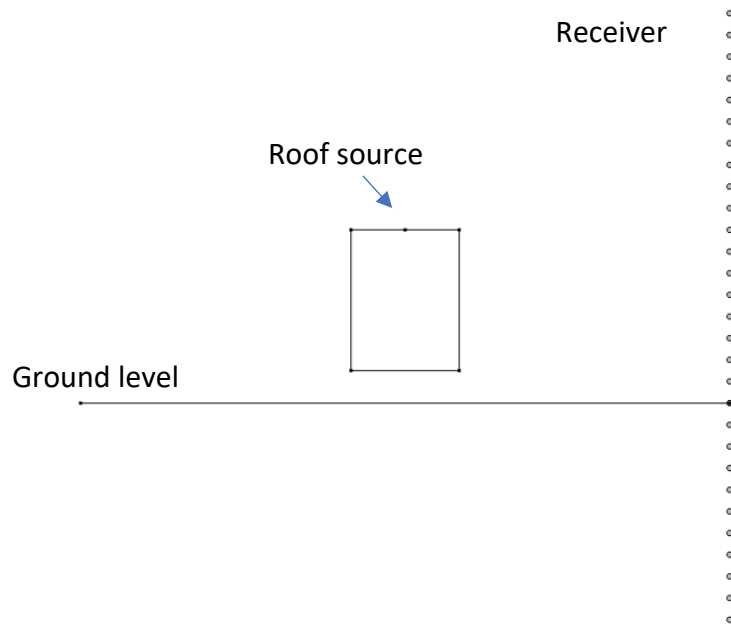
Fig. 2 The positions of the roof source and the receivers in the models

2.1.2 Boundary element models in 2D

The train geometries are modelled in 2D BE using the COMSOL software. Quadratic elements are used, with a frequency-dependent mesh giving 3.33 elements per wavelength (6.66 nodes per wavelength). The convergence of the results has been checked against a smaller mesh size with approximately double the number of elements. The source consists of a vibrating section of the train roof with width 5 mm that is embedded at the centre of the roof. A unit surface velocity amplitude is assumed for the source region.

The results from the 2D models are obtained at frequencies from 10 to 5000 Hz, with a step of 10 Hz and the complex sound pressure at each receiver height is extracted from the solutions. The ground is not included in the COMSOL models but can be considered in a post-processing step by combining the results for receivers above and below the ground level, as described in Section 3.1.2 below. However, ground reflections are not considered in the current section, but results are presented for the receivers shown in Fig. 2. Ground reflections will be introduced in Section 4.

For each train geometry, the insertion loss (IL) is calculated relative to a source in free field. The free-field results are obtained by modelling a 2D monopole as a pulsating cylinder in

7

COMSOL. The radius of the cylinder is 2.5 mm and a unit surface velocity is applied. The difference in the volume velocity compared with the train cases is taken into account in the IL calculation.

Fig. 3 shows the insertion loss results calculated from the 2D models for the four train geometries at five example receiver heights. The results are converted to one-third octave bands for ease of presentation. The IL for the receivers above the train roof are negative due to the amplification caused by the source being located on the train roof. For the receivers below the roof level (i.e. below 4 m), the IL is positive due to the shielding effect of the train body, and increases as the receiver height is reduced. Small differences can be observed between the first three train geometries, whereas there are more fluctuations in the results of the fourth train model, due to the fairing.
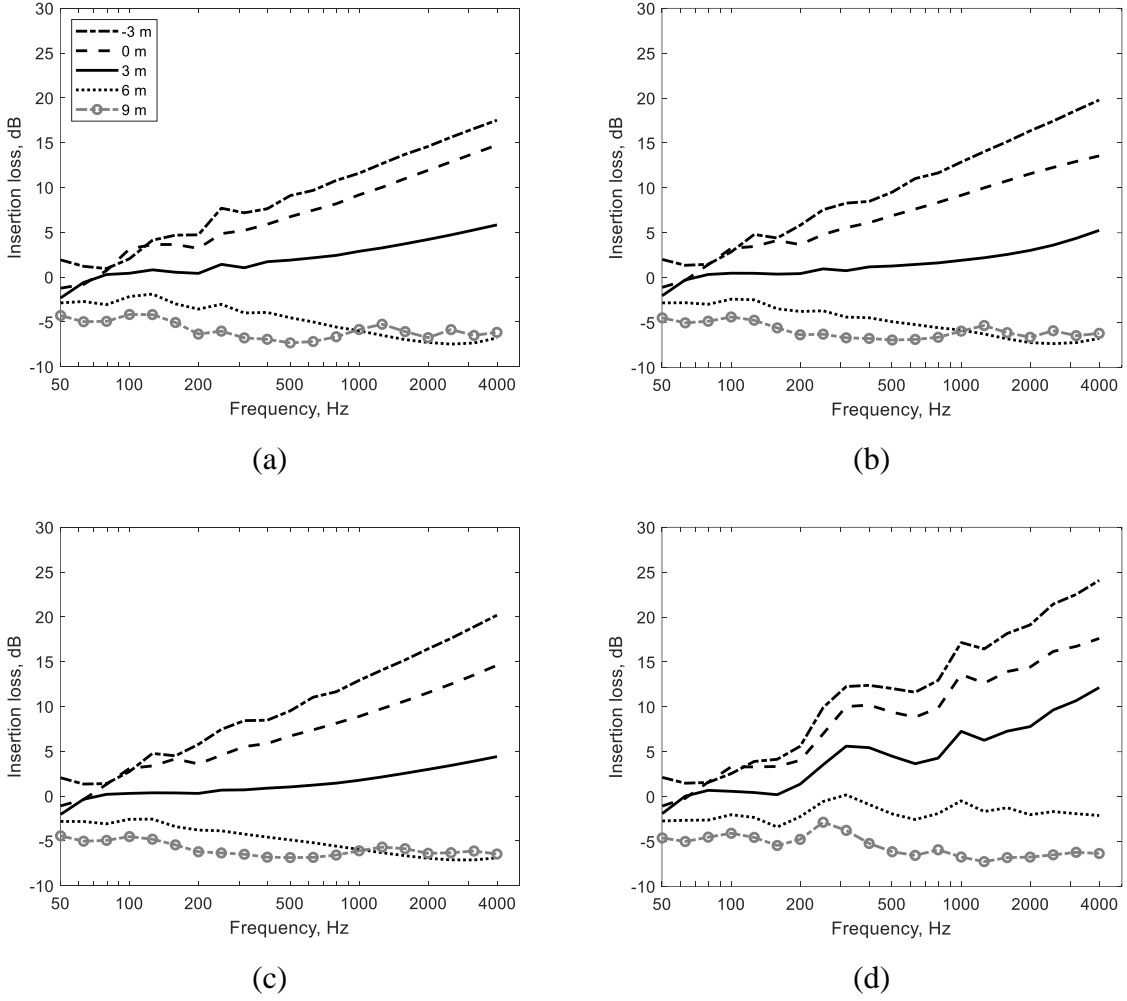
Fig. 3 Insertion loss results of the four train geometries from the 2D BE models for different receiver heights relative to the top of the rail. (a) Rectangular train geometry; (b) train roof with chamfered corners; (c) train roof with rounded corners; (d) train roof with single fairing

2.1.3 Boundary element models in 2.5D

For the roof-mounted sources, 2.5D BE models have been implemented by post-processing the output from the 2D COMSOL models described above. To apply the 2.5D method, the problem is assumed to have geometry and material properties that are invariant in the axial direction, denoted x. For each frequency, solutions are required for a range of wavenumbers k_x along the x direction. Use is made of the equivalence of solutions at pairs of circular frequency and wavenumber (ω, k_x) which share the same value of k_{2D} (the wavenumber in the y-z plane). These are related by

$$k_{2D} = \sqrt{(\omega/c_0)^2 - k_x^2} \qquad (1)$$

where c_0 is the speed of sound. The 2D solutions from COMSOL at frequency $f_{2D} = \omega_{2D}/2\pi$ correspond to wavenumbers $k_{2D} = \omega_{2D}/c_0$ and $k_x = 0$. In addition, the solution at wavenumber k_{2D} must be weighted by the factor ω/ω_{2D}, as explained in the appendix. Interpolation is used to obtain the range of solutions required. The wavenumber resolution in the longitudinal direction is set to $dk_x = 0.0016$ rad/m. The output frequencies $\omega/2\pi$ are selected from 25 Hz to 5000 Hz with a logarithmic spacing of 200 points per decade. The results are then converted to one-third octave bands for presentation.

A window function is applied to introduce a source of finite length in the axial direction in the 2.5D BE model [20]; the length is taken to be twice the width of the source in the 2D models. Finally, a Fourier transform is applied over wavenumber to obtain the results in the spatial domain over a range of values of x:

$$p(x, y, z) = \frac{1}{2\pi} \int_{-\infty}^{\infty} p(k_x, y, z) e^{-ik_x x} dk_x \tag{2}$$

The same method is applied to the reference source, which is converted from a cylindrical source to a compact source representing a monopole [20].

Fig. 4 shows examples of the IL results for the rectangular train geometry calculated from these 2.5D BE results in five example one-third octave frequency bands. The results are plotted against the longitudinal positions of the receivers from -20 m to 20 m and for receiver heights of 0 m, 3 m, 6 m and 9 m relative to the top of the rail. For receivers below the level of the train roof, the insertion loss reduces to some extent with increasing longitudinal distance due to the reduction in path length difference. The IL results at $x = 0$ are identical to those obtained from the 2D model in Fig. 3.
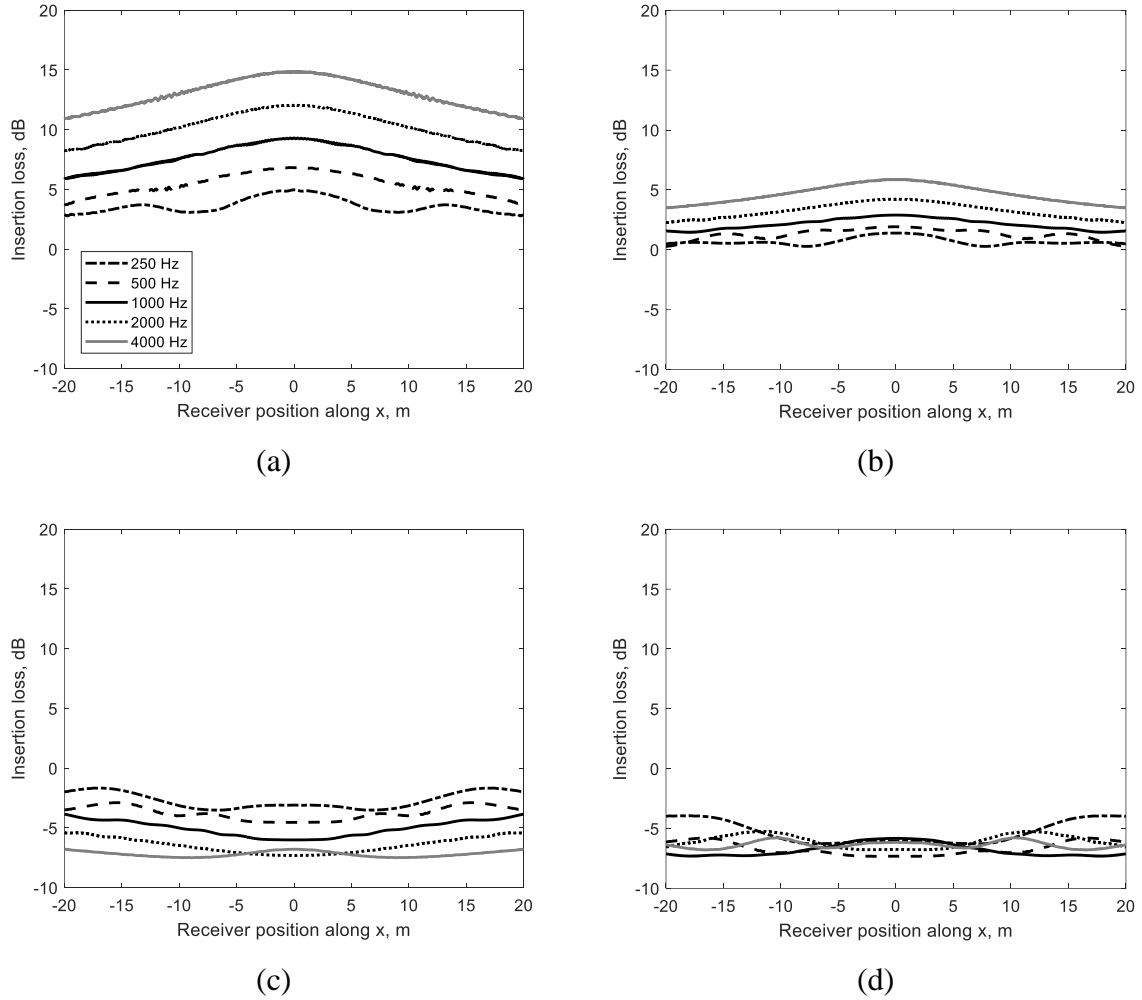
Fig. 4 Insertion loss for the rectangular train model in example one-third octave bands. Receivers at: (a) 0 m height; (b) 3 m height; (c) 6 m height; (d) 9 m height

2.1.4 Analytical model

A fast-running analytical model for the insertion loss due to the train body for a roof-mounted source is implemented by using an equivalent barrier, based on Pierce's formulation for diffraction over a thin barrier [21], see also [22]. To use this solution, the corners of the train between the source and the receiver are identified as the edges of the barrier.

In the shadow zone the sound field comprises only the diffracted field p_d, whereas in the illuminated zone it additionally contains the direct field p_i. Moreover, if the sound source is above the roof, the reflected field from the roof should also be included, as well as a diffracted component from this image source. These can be included using the formulation of

Haddon and Pierce for a wedge [23]. Limiting the discussion to the source embedded in the roof, the total sound field, p_T, is given by:

Illuminated zone:
$$p_T = p_i + p_d \qquad (3)$$

Shadow zone:
$$p_T = p_d \qquad (4)$$

Assuming a unit source strength and omitting the time-dependent factor, which is taken here as $e^{i\omega t}$, the pressure amplitude of the direct wave is given as

$$p_i = \frac{e^{-ikR_1}}{4\pi R_1} \qquad (5)$$

where k is the acoustic wavenumber and R_1 is the direct distance between the source and the receiver. For $kR' \gg 1$, the diffracted wave can be written in terms of Fresnel integrals as

$$p_d = \frac{ke^{\frac{i\pi}{4}}}{4\pi\sqrt{kR'}} \frac{se^{-ikR_1}}{\sqrt{k(R' + R_1)}} G\left(\sqrt{2N_1}\right) \qquad (6)$$

where R' is the shortest distance from the source to the receiver over the diffraction edge. The Fresnel number of the source N_1 is defined as

$$N_1 = \frac{k}{\pi}(R' - R_1) \qquad (7)$$

where $(R' - R_1)$ is the path length difference. s in Eq. (6) is equal to +1 in the shadow zone and -1 in the illuminated zone. The function $G(u)$ is defined as

$$G(u) = \int_u^\infty e^{-iu^2} du = F_r^*(\infty) - F_r^*(u) \qquad (8)$$

where $F_r^*(u)$ can be represented in terms of Fresnel integrals as

$$F_r^*(u) = C(u) - iS(u) = \int_0^u \cos\left(\frac{\pi t^2}{2}\right) dt - i\int_0^u \sin\left(\frac{\pi t^2}{2}\right) dt \qquad (9)$$

The Fresnel integrals can be approximated by using the formula in [24].

2.2 Comparison between BE and analytical results

Fig. 5 shows comparisons between the BE results and the analytical results for the receivers at five example heights at the axial position $x = 0$. The results are again converted to one-third octave bands. The BE results are given in black lines and the analytical results are in grey lines. A generally good agreement can be seen between the two sets of results above 200 Hz. Below this frequency the differences are a bit larger, which is unsurprising as the acoustic wavelength is greater than about 2 m.
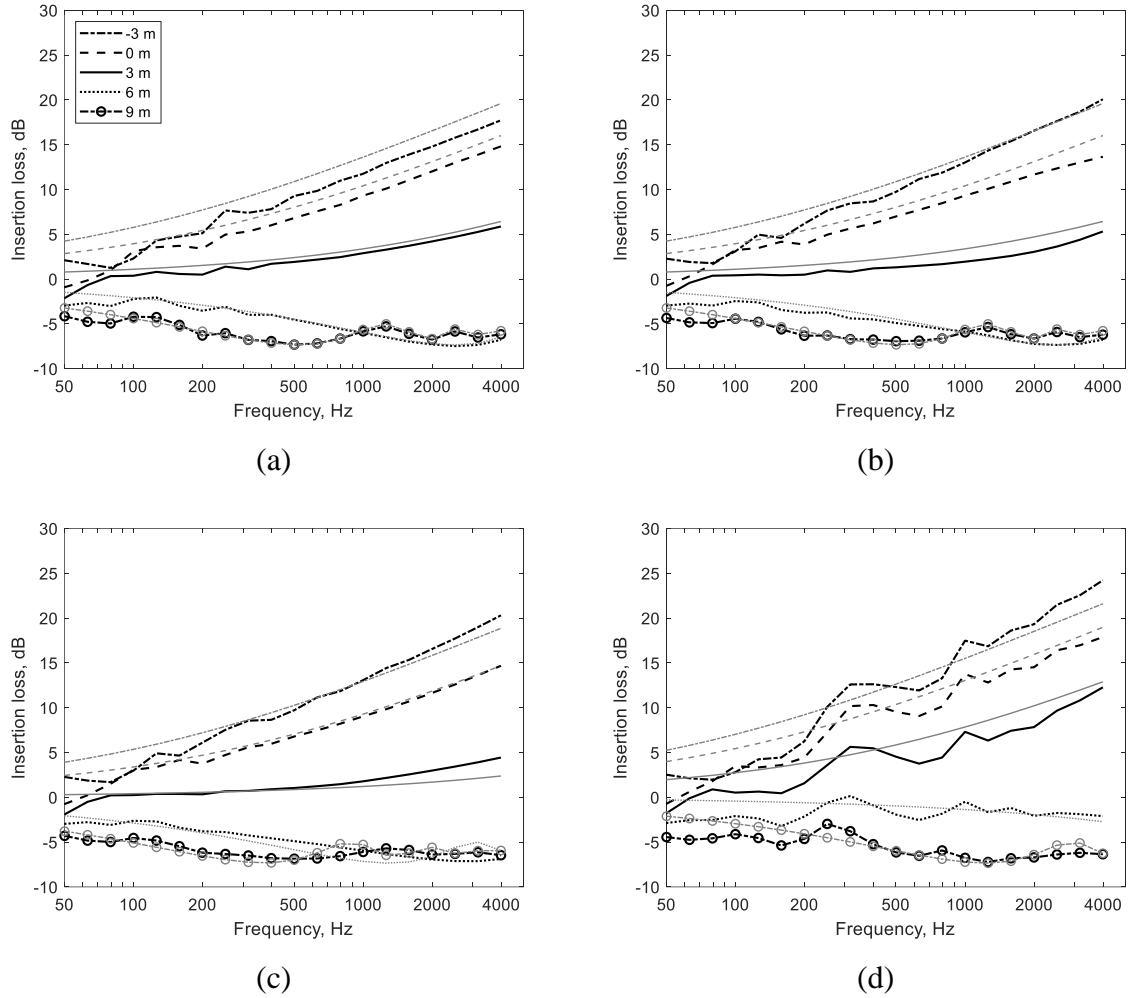
12

Fig. 5 Comparison of 2.5D BE results (black lines) and the analytical results (grey lines) in one-third octave bands at $x = 0$ for different heights of receiver relative to the top of the rail. (a) Rectangular train geometry; (b) train roof with chamfered corners; (c) train roof with rounded corners; (d) train roof with single fairing

For each train geometry, the level differences are calculated between the IL obtained with the analytical model and with the 2.5D BE model, i.e. $\mathrm{IL}_{\mathrm{analytical}} - \mathrm{IL}_{\mathrm{BE}}$. Example results for the rectangular train and the train with fairing are given in Fig. 6 and Fig. 7. In each Fig., the results are presented for two receiver heights (3 m and 6 m), five example one-third octave frequency bands and for the longitudinal positions from -20 m to 20 m. For the rectangular geometry (Fig. 6), and also the chamfered geometry (not shown), the differences are between 0 and 2 dB, indicating good agreement. For the other two train geometries there are some additional fluctuations, with differences from -2 to 3 dB for the rounded corner (not shown) and from -1 to 4 dB for the train with fairing (Fig. 7).
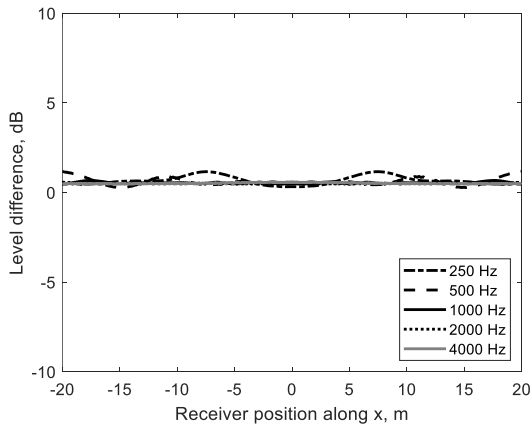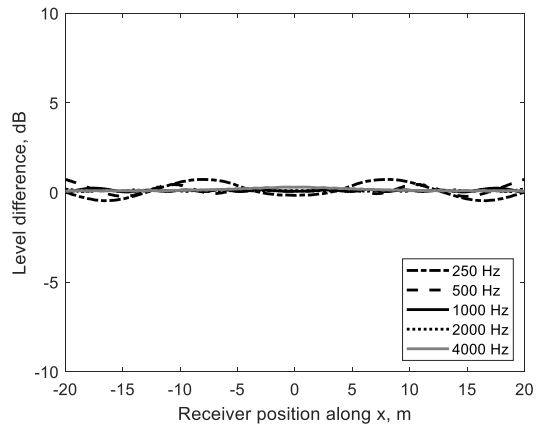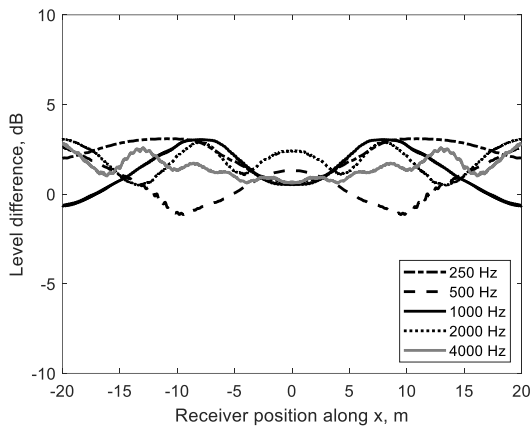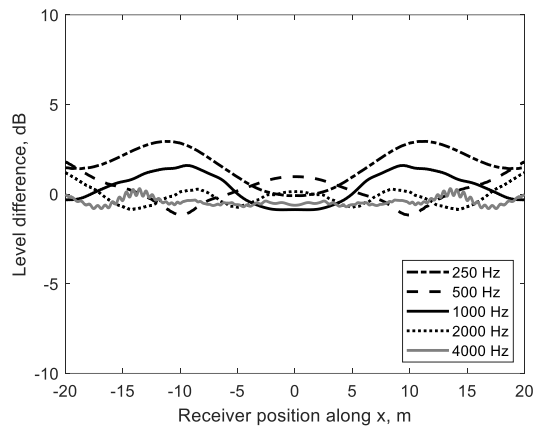
Fig. 6 Level difference between the analytical and the BE results for the rectangular train geometry in example one-third octave bands. Receiver height at: (a) 3 m; (b) 6 m

Fig. 7 Level difference between the analytical and the BE results for the train with fairing in example one-third octave bands. Receiver height at: (a) 3 m; (b) 6 m

3. Underframe-mounted sources

In this section, the sound radiation from equipment mounted beneath the train underframe is considered. A 2.5D BE model is developed for an example piece of equipment, which has a height of 0.64 m, width of 2.4 m and length of 2.1 m. In the BE model, the radiation from the various faces is represented by a series of point sources distributed across the face.

An analytical model is then developed to predict the sound radiation from this equipment. The equipment is represented as a 'box' source, with five rectangular faces; the top face is neglected as it is mounted onto the train floor. The propagation model is based on free-field

Green's functions together with a diffuse field model of the region beneath the train. This analytical model is used to calculate transfer functions of the form $L_p - L_W$, where L_p is the sound pressure level and L_W is the sound power level of the source.

3.1 BE models

3.1.1 Geometry

Similarly to the roof-mounted sources, 2.5D BE models are created for the underfloor-mounted source. Due to the required model size, different grids are used, for low, mid and high frequencies. These are shown in Fig. 8. An overlapping region was included in the frequency ranges considered using each model to ensure consistency. A ballasted track is assumed. The rails are represented by simple rectangular sections. The ballast is modelled using the Delany and Bazley model [25] with an equivalent flow resistivity of 400 kPa.s/m^2 for the sloping region and 800 kPa.s/m^2 for the flat region of the ballast. These values of flow resistivity were chosen to approximate the measured absorption coefficient of ballast [26]. For the flat region there are sleepers present over approximately 1/3 of its area, so the corresponding average absorption coefficient is reduced by a factor of 2/3, leading to this larger value of equivalent flow resistivity. The corresponding normal specific acoustic impedance is introduced as a boundary condition in the BE model.

On each face of the source, a distribution of point sources is included, achieved by using the window function as in Section 2.1.3 [20]. The transfer functions are calculated for each source separately and then combined assuming that they are uncorrelated. The bottom face has nine sources arranged in a 3×3 grid. In the lateral (y) direction these are 0.65 m apart (see Fig. 8(a)) while in the longitudinal (x) direction they are 1 m apart. The side faces (left and right) each have three sources, 1 m apart in the x direction. There are no sources located on the front and the rear faces, as they cannot be represented in a 2.5D model. Instead, the two rows of sources near the edges of the bottom face are used to represent the front and the rear faces as well.
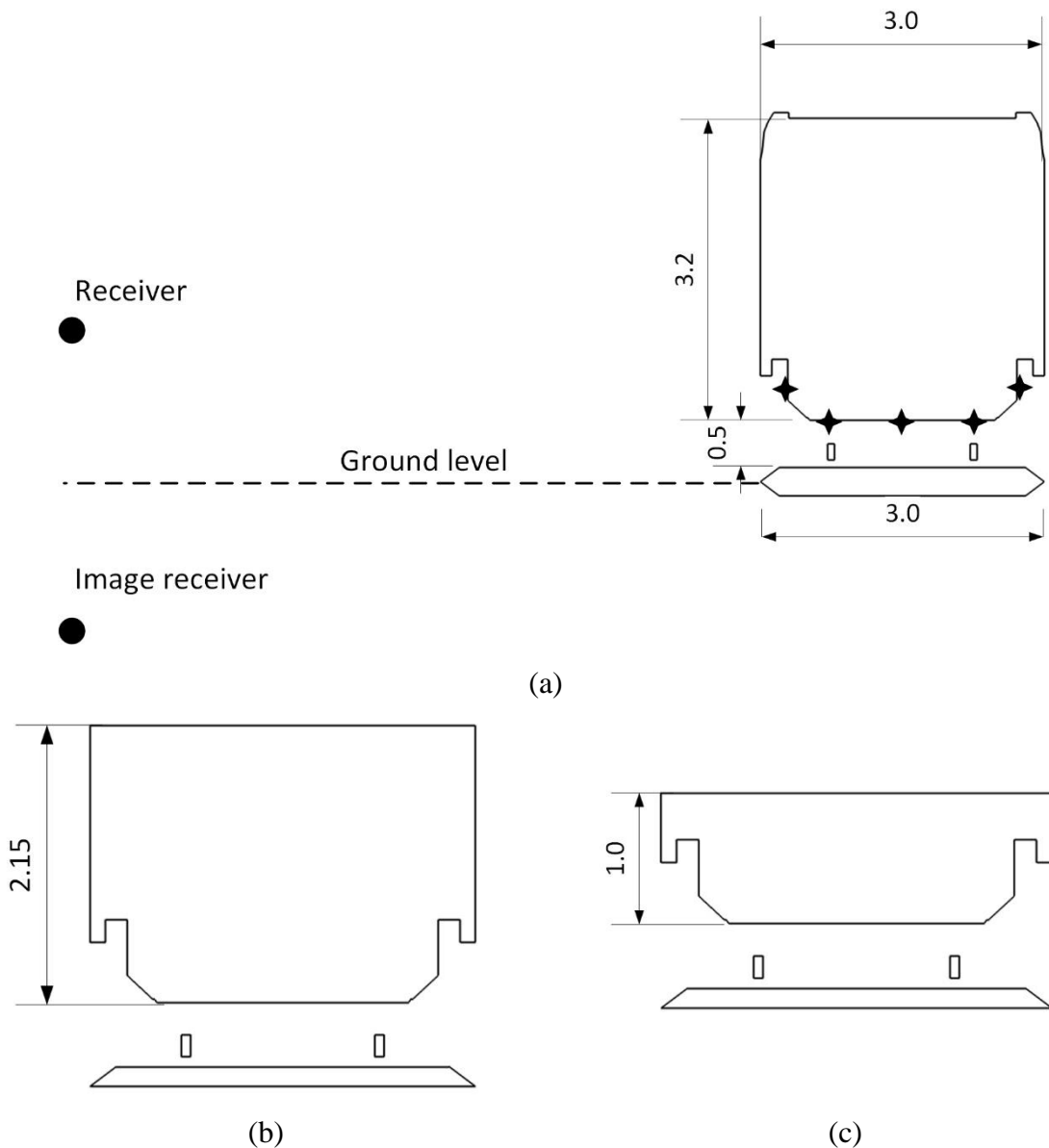
Fig. 8 Cross-section of the train-track models with main dimensions shown in m. (a) Low frequency model, used up to 400 Hz), with maximum element size of 0.125 m, showing locations of sources (shown by the star symbols) and receivers (not to scale); (b) mid-frequency model used up to 1.4 kHz, with maximum element size of 0.09 m; (c) high frequency model, with maximum element size of 0.03 m

3.1.2 Ground reflection

Ground reflections in the far field are considered by means of image receiver points, i.e. points located symmetrically beneath the ground level. The ground surface is assumed to be flat and horizontal. The total pressure including the ground reflection p_{total} can be calculated

from the complex free-field pressure amplitudes at the receiver p_{rec} and at the image receiver p_{im} as [27]

$$p_{\text{total}}(x, y, z) = p_{\text{rec}}(x, y, z) + R(\phi)\, p_{\text{im}}(x, y, z) \qquad (10)$$

where $R(\phi)$ is the amplitude reflection coefficient, which can be expressed in terms of the ground impedance [27]:

$$R(\phi) = \frac{(z_n' \cos \phi - 1)}{(z_n' \cos \phi + 1)} \qquad (11)$$

where ϕ is the incident angle relative to the normal, which can be calculated as

$$\phi = \frac{\pi}{2} - \tan^{-1} \frac{z_{\text{rec}} + z_{\text{srce}}}{\sqrt{(x_{\text{rec}} - x_{\text{srce}})^2 + (y_{\text{srce}} - y_{\text{rec}})^2}} \qquad (12)$$

with (x, y, z) representing the coordinates of the receiver (rec) and source (srce) in longitudinal, lateral and vertical directions. In Equation (11), $z_n' = z_n/\rho_0 c_0$ is the non-dimensionalised normal specific acoustic impedance. The ground impedance, z_n, is estimated using the Delany and Bazley model [25] with an equivalent flow resistivity of 50 kPa.s/m^2. It has been verified that, for these angles, there is no need to include the spherical reflection coefficient.

3.2 Analytical models

For practical use, a fast-running analytical model is developed for the underframe mounted source. For the side face of the source, free-field (half-space) Green's functions are used, i.e. the transfer functions are estimated for a series of point sources in a half space. For the bottom face of the source, the region beneath the train is represented by a diffuse field model. The propagation to the receiver is then calculated using a similar half-space Green's function approach. Ground reflection is included using a similar approach to the numerical model, described in Section 3.1.2.

3.2.1 Side face

For sources on the side of the equipment, there is minimal obstruction in the transmission path when the receivers are on the same side of the train as the source region. The diffraction from the model geometry is assumed to be small and is neglected here, although the diffraction model from Section 2 could be used if needed. For a point source in a half space

(defined by the side face of the source), assuming a time-dependent factor of $e^{i\omega t}$, the pressure is given by

$$\frac{p(r)}{q} = i\omega\rho_0 \left(\frac{e^{-ikr}}{2\pi r}\right) \tag{13}$$

where r is the distance (in 3D) between the point source and the receiver, q is the volume velocity of the point source, ρ_0 is the density of air and k is the acoustic wavenumber. The sound power for the point source in a half space is related to the volume velocity by [28]

$$W = \rho_0 c_0 k^2 |q|^2 / 4\pi \tag{14}$$

When the receivers are on the opposite side of the train, the side faces have a much smaller contribution (10 – 15 dB lower than the total value). Therefore, this component is omitted from the analytical model.

Similar to the 2.5D BE model, three point sources are distributed on the side face of the source box in the x direction, at 1 m intervals. The transfer functions are energy-averaged over the three point sources.

3.2.2 Bottom face

Unlike the side face, the bottom face of the equipment is close to the track and has no direct line of sight to the receiver. As shown in Fig. 9, a partial cavity is formed by the bottom face of the source, the ballast and the gaps between the bottom face and the rails. The sound power which is radiated from the gaps is denoted W_{rad}.
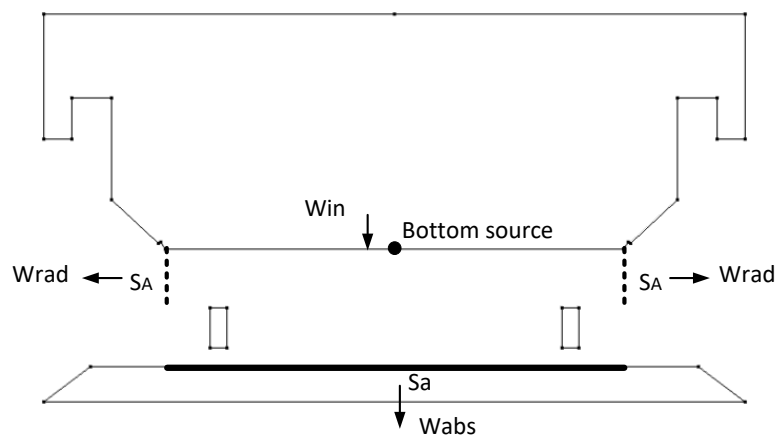

Fig. 9 The cavity beneath the train and the sound power flow for the bottom face

The sound field in the cavity beneath the train is complicated and may be considered to consist of a diffuse field and a direct field. The sound radiated by a point source within a certain angle will reach the ballast from which it is partially reflected and partially absorbed (the power which is absorbed is denoted W_{abs}). This is shown as region A in Fig. 10. This is assumed to generate a semi-reverberant (diffuse) field. The fraction of the sound power W_{in} emitted by the source that enters region A may be approximated from the angle θ_1 (for the centre source) and θ_2 (for the side source) divided by π. For the geometry in Fig. 9, the proportion η entering the diffuse field estimated from the average over different source positions, is 78%.
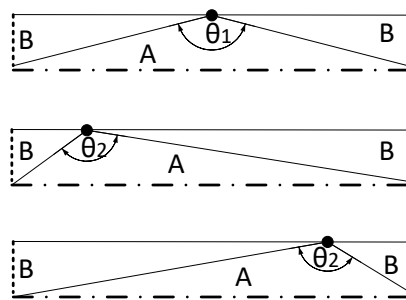

Fig. 10 The diffuse field (A) and the direct field (B) in the cavity. The diffuse field contributions for the central source and the side sources are marked by θ_1 and θ_2. The rail height is excluded

For the diffuse field, region A, an insertion loss is evaluated to account for the absorption at the ballast. Region A can be effectively treated as a simple noise control enclosure [28]. The aperture areas are the gaps at both sides of the train, marked by the dotted lines ($2 \times S_A$) in Fig. 10. The ballast area, marked by the dash-dotted line (S_a) in Fig. 10, is assigned a diffuse field absorption coefficient α_d, which is determined using the Delany and Bazley model [25] with an equivalent flow resistivity of 800 kPa.s/m^2, as above.

The insertion loss (IL) of the diffuse field part of the cavity can be estimated as [28, 29]

$$IL = 10 \log_{10} \frac{S_a \alpha_d + 2S_A}{2S_A} \tag{15}$$

The diffuse sound power emitted on both sides of the train is

$$W_{\text{diff}} = \eta W_{in} \times 10^{-IL/10} \tag{16}$$

whereas the direct field part on both sides is

$$W_{\text{dir}} = (1 - \eta)W_{in} \tag{17}$$

19

Hence the overall insertion loss is

$$IL_{\text{total}} = 10 \log_{10} \frac{W_{\text{in}}}{W_{\text{rad}}} = -10 \log_{10} \left((1 - \eta) + \eta \times 10^{-\frac{IL}{10}} \right) \tag{18}$$

Half the sound power is emitted on each side of the train, so the sound power level emitted on one side of the train is given by

$$L_{W_{\text{rad1}}} = L_{W_{\text{in}}} - IL_{\text{total}} - 3 \tag{19}$$

Fig. 11(a) shows the estimated insertion loss. The IL applying to the diffuse field in the cavity (equation (15)) is represented by the dashed line; it has a range of $0 - 5$ dB. The total insertion loss, accounting for the contribution from the direct field (equation (18)), is shown as the solid line. It is smaller than the IL applying to the diffuse field, because the direct field part is not attenuated. Note that, if a slab track is used, the values of IL will be much smaller.
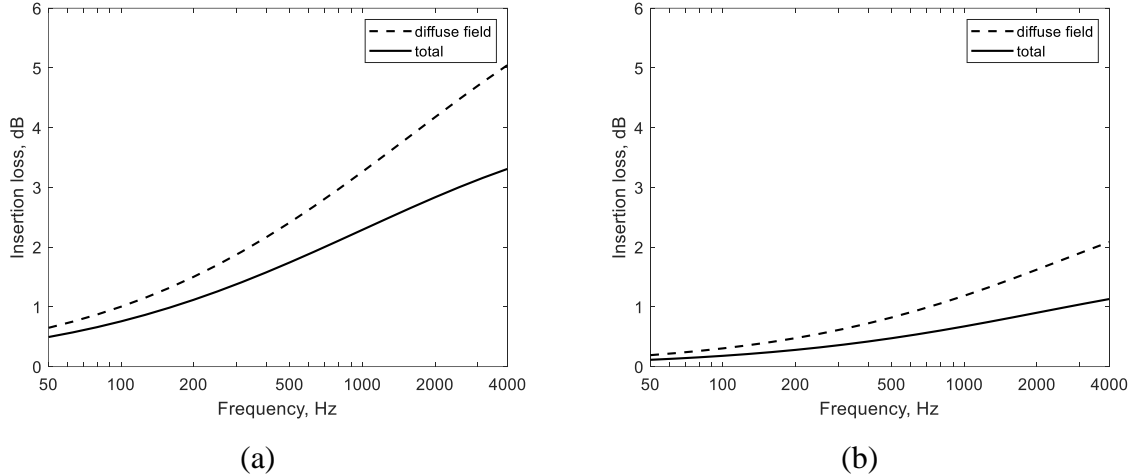

Fig. 11 (a) Estimated insertion loss for the bottom face; (b) estimated insertion loss for the front and the rear faces

The total power radiated from one side of the cavity (from regions A and B) is assumed to propagate to the receivers on this side of the train from an equivalent point source, using the same method as for the side sources, including ground reflections. The equivalent point sources are located at the centre of gap, shown by dotted lines in Fig. 9. Three sources are distributed along the x direction.

3.2.3 Front and rear faces

The front and rear faces of the equipment radiate into a tall narrow cavity between the source and any adjacent equipment under the train. A similar method is used as for the bottom face. The percentage of the power entering the diffuse field, averaged over three source positions, is calculated as 60% in this example.

Fig. 11(b) shows the estimated insertion loss for the end faces of the equipment. The IL applying to the diffuse field in the cavity is shown as the dashed line. As the frequency increases it increases to around 2 dB at 4 kHz. The total insertion loss, accounting for the contribution from the direct field, is shown as the solid line.

Similar to the case of the bottom face, the total power radiated from one side of the cavity (from regions A and B) is assumed to propagate to the receivers on this side of the train from an equivalent point source, using the same method as for the side sources. This equivalent point source is again located at the centre of gap.

3.3 Comparison with 2.5D results

The transfer functions obtained from the analytical model described above are compared with those from the 2.5D BE model, shown in Fig. 8. The receiver positions are identified as R1 – R4. These are located at 7.5 m from the track centreline on both sides, and spaced 3 m apart, with position 1 ($x = 0$) aligned with the centre of the side face of the equipment. For each receiver position, there are two microphone heights, the lower one at 1.2 m and the higher one at 3.5 m, measured from the rail head. The ground height is 0.4 m below the rail head.

Fig. 12 shows the transfer functions for the side faces, compared with the 2.5D results. Two examples are shown, for positions R1 and R3 ($x = 0, 6$ m) at the lower microphone height. The results are presented as $L_p - L_W$. The transfer functions are averaged over the three source positions located on this face. A good agreement is found between the analytical model results and the 2.5D results for most frequencies and positions, with average absolute differences of 2 dB in each case. The largest differences occur around the ground dip at 300-500 Hz and around 2 kHz.

The sensitivity of the results to the number of sources used for this face has been investigated. It has been shown that the three-source arrangement has a reasonably good agreement with the arrangement with more sources.
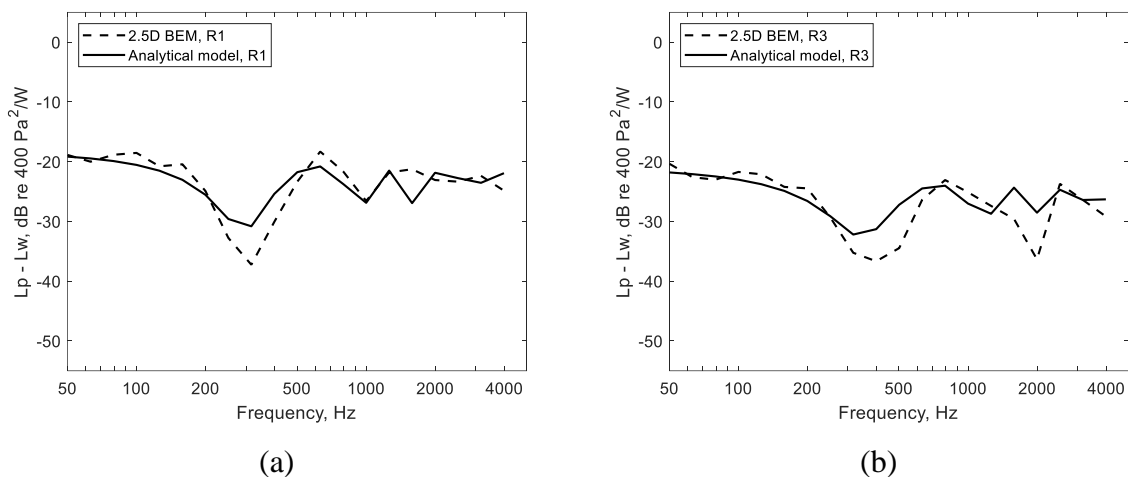

(a)   (b)

Fig. 12 Comparison of the transfer functions ($L_p - L_W$) for the side faces (left or right) between the analytical model results and the 2.5D BE results when the source and the receivers are on the same side. (a) Position R1 ($x = 0$ m, height 1.2 m); (b) position R3 ($x = 6$ m, height 1.2 m)

Fig. 13 shows the overall transfer functions ($L_p - L_W$) for the bottom face obtained from the analytical model results and the 2.5D BE results. These results are averaged over 9 source positions on the bottom face in the 2.5D BE method. In the analytical model, three lateral source positions (see Fig. 10) are used to determine the factor η and then three longitudinal positions are used for the equivalent sources in the gap (Fig. 9) to calculate the free-field propagation. A generally good agreement is found between the two sets of results for most frequencies and positions, again with average absolute differences of 2 dB. Larger differences are found below 100 Hz and in the region 250-500 Hz. A similar level of agreement was also obtained for the end faces.
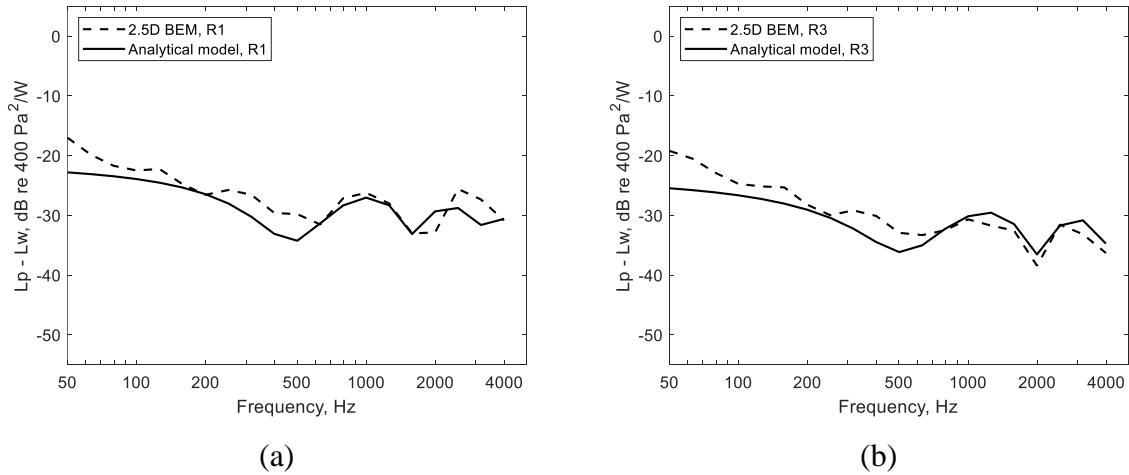
Fig. 13 Comparison of the transfer functions ($L_p - L_W$) for the bottom face between the analytical model results and the 2.5D BE results. (a) Position R1 ($x = 0$ m); (b) position R3 ($x = 6$ m)

3.4 Sound pressure levels

The transfer functions estimated from the analytical and BE models are used to calculate the sound pressure levels at the receiver positions by combining the contributions from each face. For this, sound power spectra from each face of the equipment are used that were measured previously in a laboratory set-up [30].

Fig. 14 shows the level differences between the results from the analytical model and the 2.5D BE model for receivers on the right side of the train. The two models agree well at low frequencies but the level difference generally increases at the higher frequencies, especially when the receiver position is located further away from the source and at the higher receiver location. Results for the receivers on the left side (not shown) are similar.
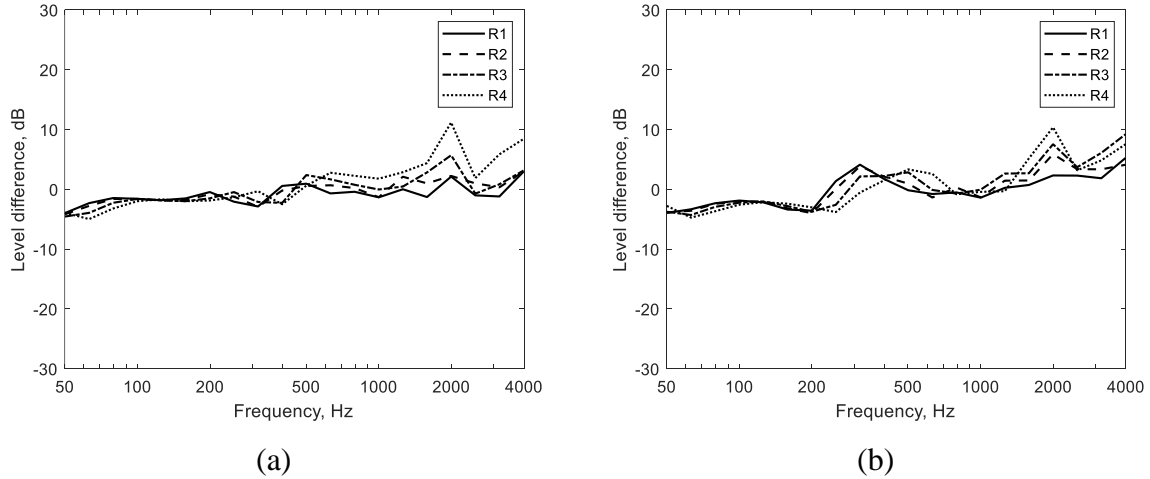
(a)   (b)

Fig. 14 Level difference between the sound pressure predicted using the analytical model and
the 2.5D BE model for the receivers on the left at (a) the lower microphone height of 1.2 m
and (b) the higher microphone height of 3.5 m above the rail head

4. Analysis of uncertainties

This section discusses the uncertainty in the predictions for both roof-mounted and
underframe-mounted sources. Modelling uncertainty is assessed by comparing the results
from the analytical models with the more accurate 2.5D BEM model. For the underframe
source, comparisons are also made with measurements. Parametric uncertainty is addressed
by varying the input parameters in the analytical model.

4.1 Roof-mounted sources

4.1.1 Modelling uncertainty: differences between analytical and BEM models

For roof-mounted sources, the modelling uncertainty can be estimated by comparison of the
results from the analytical model with those from the 2.5D BEM model.

Fig. 15 shows the uncertainty range (mean $\pm 2\sigma$, where σ is the standard deviation in each
frequency band) plotted against one-third octave frequency band. These results are based on
the level differences between the analytical and the BE results for all four train models in Fig.
1 and all receivers (in both the longitudinal direction, [-20 20] m, and the vertical direction
[-5 9] m). The standard deviation is around 1 dB. The mean differences are greater at low

frequency: the average (over frequency) of the mean differences at low frequency (50-200 Hz) is 1.7 dB, whereas the average of the mean differences at higher frequency (250-4000 Hz) is 0.5 dB.
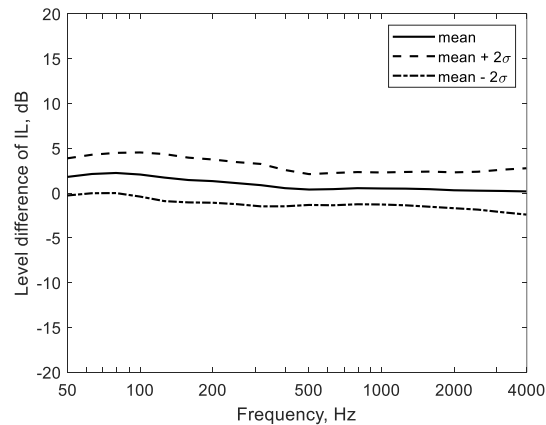

Fig. 15 Level differences in the IL between the analytical and the BE results for roof-mounted sources as a function of frequency (four train geometries, receiver heights [-5 9] m, longitudinal positions [-20 20] m)

The uncertainty range (mean $\pm 2\sigma$) has also been calculated separately for each longitudinal receiver position, although for brevity the results are not shown. The mean difference is found to be almost independent of longitudinal position.

Fig. 16 shows the uncertainty range (mean $\pm 2\sigma$) plotted against receiver height. These results include all four train models, all longitudinal receiver positions and all frequency bands. Results are shown separately for low frequency bands (50-200 Hz) and high frequency bands (250-4000 Hz). The mean difference is close to 0 dB for the high frequency bands (average value 0.5 dB) and the $\pm 2\sigma$ range is also mostly smaller than at low frequency, except for positions below -3 m. For the low frequency bands, the average of the mean difference over all receiver heights is 1.8 dB.
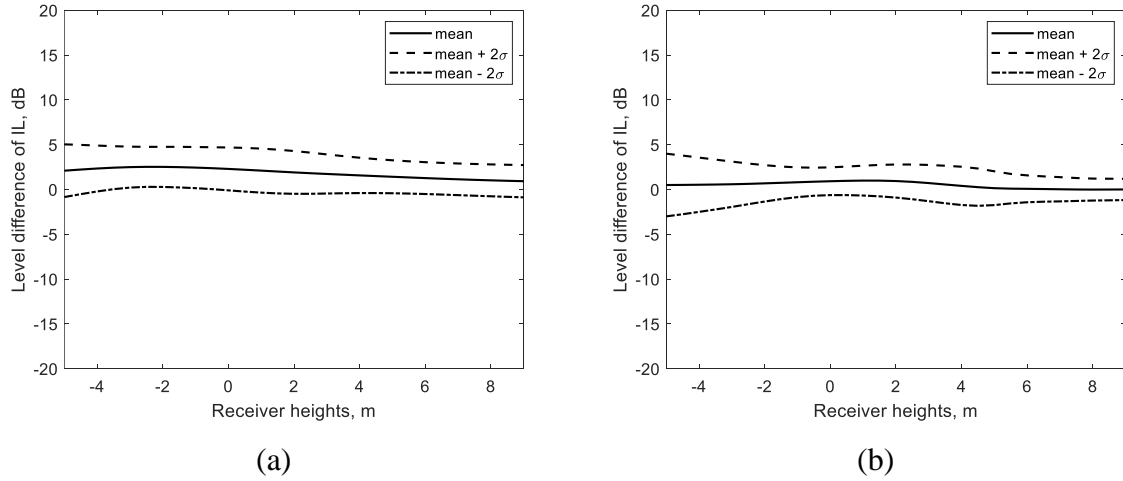
(a)   (b)

Fig. 16 Level differences of the IL between the analytical and the BE results for roof-mounted sources plotted against receiver height (four train geometries, longitudinal positions [-20 20] m). (a) Frequency bands 50-200 Hz; (b) frequency bands 250-4000 Hz

4.1.2 Parametric uncertainty: differences using analytical model

Parametric uncertainty for roof-mounted sources is assessed by considering variations in train geometry and in ground properties using the analytical model. Similar to the results in Section 3, the ground reflections are now added using an image receiver and amplitude reflection ratio calculated from the ground impedance. All combinations of the following parameter variations are considered using the analytical model:

- Ground height: 0.4, 0.65, 0.9, 1.15 and 1.4 m below rail head
- Ground flow resistivity: 1×10^5, 3×10^5, 1×10^6 and 3×10^6 Pa.s/m^2
- Receivers at $x = 0$, 3, 6 and 9 m
- Receiver heights: 1.2 and 3.5 m above rail
- Lateral source position: $y = 0$, 0.5 and 1.0 m (from train centre)
- Position of diffraction edge: 8 positions, as listed in Table 1. Configurations 1, 4, 5 and 7 correspond to the geometry considered in Section 2.

26

Table 1. Coordinates of corner positions.

	y (m)	z (m)
1. Rectangular geometry	1.25	4.0
2. Wider rectangular geometry	1.35	4.0
3. Wider rectangular geometry	1.45	4.0
4. Rounded geometry	1.4	3.95
5. Middle of chamfered edge	1.35	3.9
6. Small fairing	1.25	4.1
7. Top of fairing	1.2	4.25
8. Alternative fairing	1.25	4.2

Restricting the configurations to a single corner location and single source position, Fig. 17 plots the mean and $\pm 2\sigma$ range of the insertion loss over all receivers, ground heights, and ground impedances. For the lower receivers, at 1.2 m above the rail, the results shown in Fig. 17(a) contain considerable variation at low frequencies caused by variations in the position of the ground dip. This shows the importance of correct estimates of the ground properties, particularly its height relative to the rail. Above 1 kHz the variability is small. For the upper receivers, at 3.5 m above the rail, Fig. 17(b), the ground dip affects the results only below 300 Hz, above which the variability is very small.

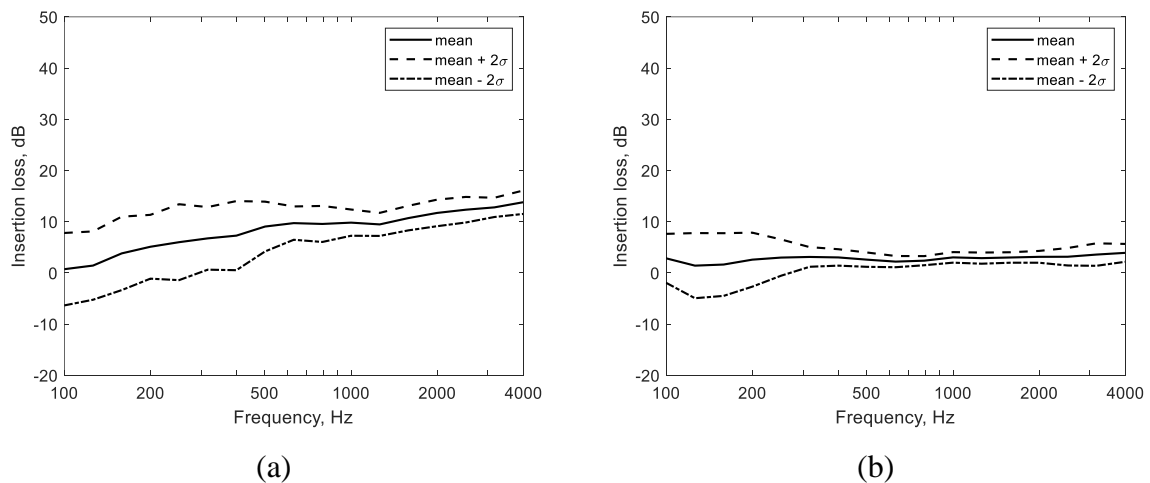(a)   (b)

Fig. 17 Range of the insertion loss predicted using the analytical model for roof-mounted source using only a single corner position and single source location. (a) Lower receivers; (b) upper receivers

Fig. 18 shows the corresponding results when all 8 corner locations and all three source positions are considered. Compared with Fig. 17 the variability at high frequencies is increased, especially for the upper receivers, at 3.5 m height, which are quite close to the height of the roof. These results indicate the importance of suitable choices for the location of the diffraction corner and source location.
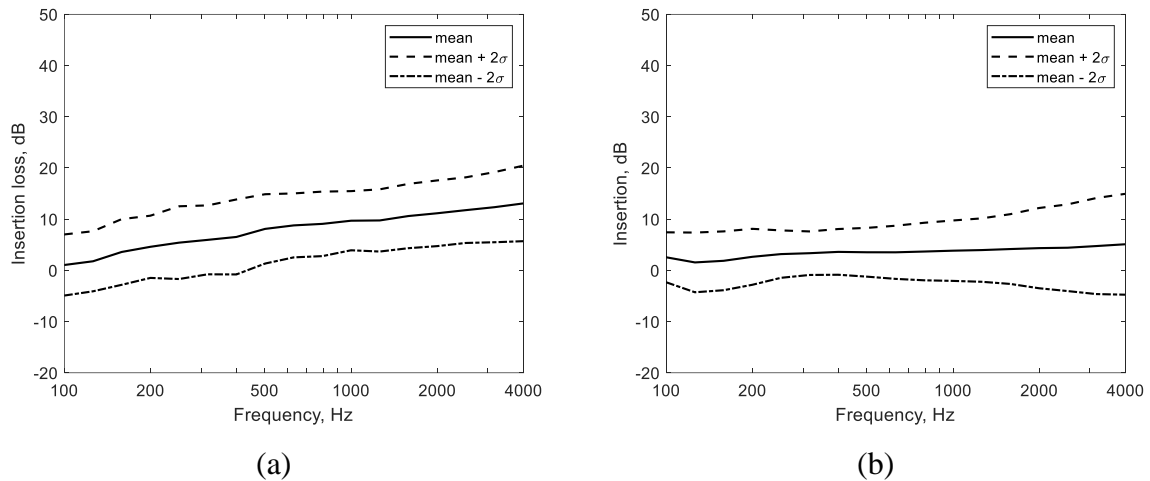

(a)   (b)

Fig. 18 Range of the insertion loss predicted using the analytical model for roof-mounted source. (a) Lower receivers; (b) upper receivers

Fig. 19 compares the standard deviation of these results when based on one or all 8 corner positions and when based on only the central source position ($y = 0$) or all 3 source positions. For the lower receivers the standard deviation is 3-4 dB for frequencies up to 400 Hz, due to the variations in the position of the ground dip, whereas for the upper receivers the ground dip occurs at lower frequencies and the standard deviation is less than about 3 dB at low frequency and reduces above 200 Hz. When the different corner positions are included, the standard deviation increases at high frequency, especially for the upper receivers. Considering the multiple source positions also leads to an increase in the standard deviation at higher frequencies but a small reduction at low frequencies.
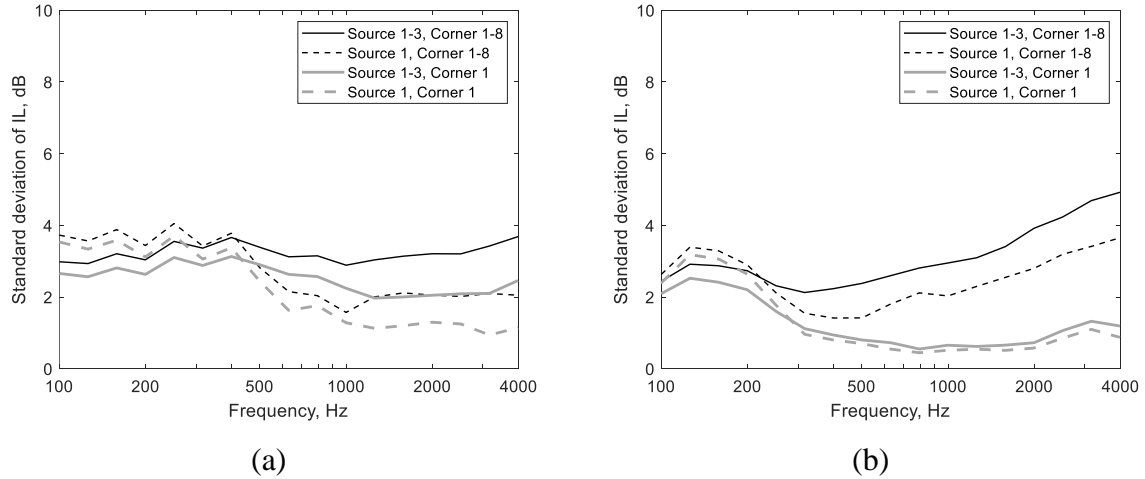
Fig. 19 Standard deviation of the insertion loss predicted using the analytical model for roof-mounted source. Comparison of results for a single location of the diffraction corner and all 8 locations, and for a single source position and 3 positions. (a) Lower receivers; (b) upper receivers

4.2 Underframe-mounted sources

4.2.1 Modelling uncertainty: differences between models and measurements

For underframe-mounted sources, the modelling uncertainty can be estimated by comparison of the results from the analytical model, the 2.5D BEM model and measurements.

Fig. 20(a) shows the uncertainty range (mean $\pm 2\sigma$) based on the level differences for all receivers between the analytical model and the BE model, such as those shown in Fig. 14. The mean difference between the analytical model and the 2.5D BE model is within ± 1 dB between 250 and 1250 Hz. At low frequencies the results from the analytical model are on average up to 4 dB lower than the BE model and at high frequencies they are up to 5 dB higher. The differences at low frequencies are mainly due to the bottom and end sources, whereas the side source gives good agreement with the BE model (see Figs 12 and 13). The differences at high frequencies are mainly due to the furthest receiver at 9 m (see Fig. 14) and are greater for the upper receivers than for the lower ones. Here, there may be some shielding present in the BE model as the source height used for the side sources is rather close to the bottom of the fairing. The standard deviation is less than 1 dB below 200 Hz and around

1000 Hz. It is larger at the ground dip around 300 Hz and above 1.6 kHz, with a maximum value of 3 dB at 2 kHz.

The noise due to the equipment, when it is installed under the train, has also been measured at the receiver locations identified in Section 3.3 [31]. Fig. 20(b) shows the uncertainty range (mean $\pm 2\sigma$) based on the level differences between the analytical model and the measurements. The average of the mean difference over all frequency bands is 0.4 dB. The standard deviation of these mean differences is 3.0 dB. The large difference observed at 2 kHz is associated with differences in operating conditions of the equipment in the sound power [30] and sound pressure [31] measurements. The standard deviation over the different measurement positions σ varies from 1 dB to 4 dB.
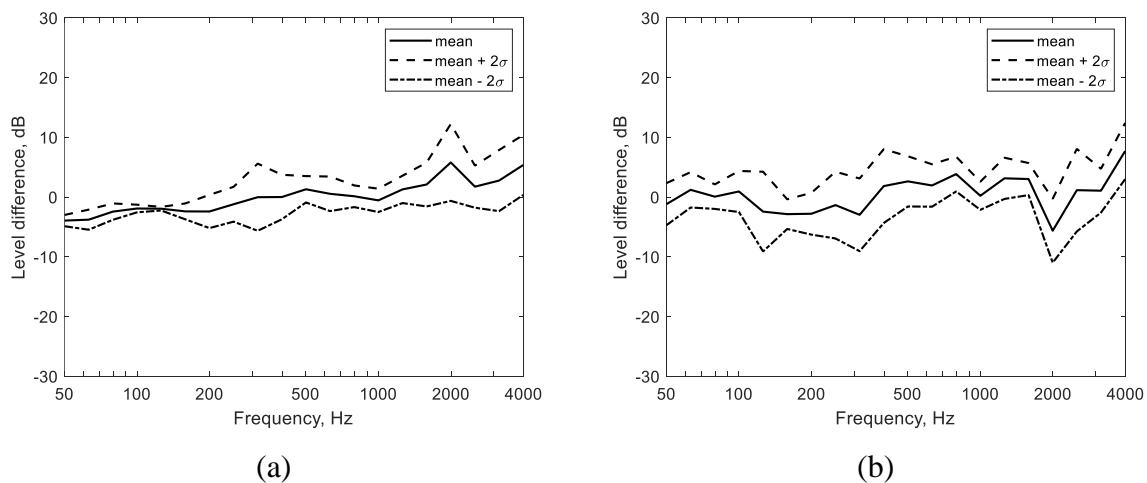

(a)   (b)

Fig. 20 Range of the sound pressure level difference between the predictions and the measurement for all the receivers for underframe-mounted equipment. (a) Analytical model compared with BE model; (b) analytical model compared with measurement

4.2.2 Parametric uncertainty: differences using analytical model

Parametric uncertainty for underframe-mounted sources is assessed by considering variations in train and source geometry and ground properties on the sound pressure level. All combinations of the following parameter variations are considered in the analytical model:

- Ground height: 0.4, 0.65, 0.9, 1.15 and 1.4 m below rail head
- Ground flow resistivity: 1×10^5, 3×10^5, 1×10^6 and 3×10^6 Pa.s/m^2
- Receivers R1 – R4 (i.e. $x = 0$, 3, 6 and 9 m) on both sides of the train
- Receiver heights: 1.2 and 3.5 m above rail

- Gap between the rail head and the bottom of the equipment: 0.89 m and 0.94 m
- Absorption coefficient of the ballast: measured absorption coefficients are considered as well as the calculated ones used in the BE model.

Fig. 21 shows the standard deviation of the sound pressure level for each receiver. The standard deviations are up to 4 dB at low frequency, reducing to around 1 dB at high frequency. The lower receivers, for which the large variations extend up to 500 – 800 Hz, are again more affected by the position of the ground dip than the upper receivers. These results indicate the importance of reliable estimates of ground height in particular.
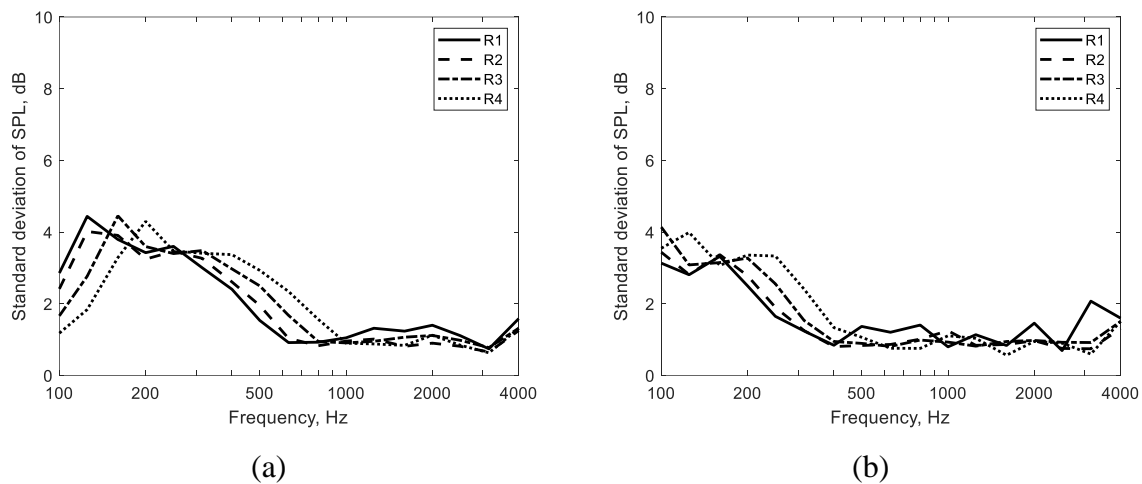

(a)   (b)

Fig. 21 Standard deviation of the sound pressure level from the predictions for underframe-mounted equipment. (a) Lower receivers; (b) upper receivers

4.3 Discussion

The results of the uncertainty study are summarised in Table 2. The largest variability occurs due to the position of the ground dip, especially for the lower receiver. This leads to large standard deviations of up to 4 dB at low frequencies. For the roof-mounted sources, uncertainty over the location of the diffraction corner can also lead to large standard deviations. If the ground height and the corner and source positions are known reliably this uncertainty can be largely controlled.

There are a number of other sources of uncertainty that could not be considered in the current study. There will be differences between nominally identical pieces of equipment for which

there is a lack of information. There may also be variation in the operating point of equipment.

The measurement accuracy and measurement environment during the sound power measurements will introduce uncertainty into the predictions, which are based on these measurements. Source directivity has not been included in the models apart from identifying the sound power from each face. Moreover, it has been assumed that the sources are evenly distributed over the faces but, in reality, they may be localised due to the position of fans, etc.

The diffraction model gives correct results for simple train geometries, but does not take account of complex shielding arrangements, such as reflections between the source and fairing, or the effect of slits in the fairings. The ground reflections have been calculated assuming a flat ground topology. Realistic ground profiles would affect the reflected sound, but the range of results obtained with varying ground height and impedance gives an indication of the likely effect.

Table 2. Summary of uncertainty results.

	Roof sources	Underframe sources
Modelling uncertainty		
Mean, 50-200 Hz	1.7 dB	-3 dB
Mean, 250-1250 Hz	0.5 dB	0 dB
Mean, 1600-4000 Hz	0.5 dB	3 dB
σ, 50-200 Hz	1 dB	0.6 dB
σ, 250-1250 Hz	1 dB	1.5 dB
σ, 1600-4000 Hz	1 dB	2.4 dB
Parametric uncertainty		
σ, lower receivers, low frequency	3-4 dB ($\leq$400 Hz)	3-4 dB ($\leq$500 Hz)
σ, upper receivers, low frequency	2-3 dB ($\leq$200 Hz)	3 dB ($\leq$300 Hz)
σ, higher frequencies (lower or upper receivers) for single corner / source position	0.5-1 dB	1 dB
σ, higher frequencies (lower or upper receivers) over multiple corner / source positions	2-5 dB	n/a

5. Conclusions

Simplified, fast-running analytical models have been introduced to account for installation effects in the transmission path for auxiliary equipment mounted on the roof or in the underframe of a train.

For sources on the roof, an analytical model based on diffraction over a thin barrier is used. Compared with 2.5D boundary element models, the results are within 2 dB above 200 Hz for simple train geometries. For more complex train geometries there are some additional fluctuations in the BE results, with differences from -2 to 3 dB for a rounded corner and from -1 to 4 dB for a train with a fairing.

For sources mounted under the train, analytical models have been developed for the transfer functions from sound power level of each face of a box source to the sound pressure level at the trackside receivers. For the side face this model is based on free-field Green's functions

and good agreement is found with the 2.5D BE model, with mean absolute differences of 2 dB. For the bottom face, it is assumed that the power is emitted first into a semi-reverberant cavity and then free-field Green's functions are used for transmission to the receivers. A similar level of agreement is obtained with the 2.5D BE model as for the side face.

Uncertainty is studied in terms of modelling uncertainty and parametric uncertainty. The largest variability occurs due to the position of the ground dip, especially for the lower receiver. For the roof-mounted sources, uncertainty over the location of the equivalent barrier can also lead to large standard deviations. The uncertainty can be largely controlled if the ground height and the corner and source positions are known reliably. Uncertainty due to the source could not be quantified in the current study but may include differences between nominally identical pieces of equipment, variation in operating point of the equipment, directivity and distribution of sources over each surface.

Appendix: calculation of 2.5D solution from 2D solutions

Assuming time-harmonic variations with dependence $e^{i\omega t}$ (where i is the imaginary unit and ω is the angular frequency), the 2.5D boundary integral equation is

$$\tilde{p}(k_x, y', z') = -\int_\Gamma \left(i\rho\omega\tilde{v}(k_x, y, z)\psi(k_x, y, z|y', z') + \tilde{p}(k_x, y, z)\frac{\partial\psi(k_x, y, z|y', z')}{\partial n} \right) d\Gamma \tag{A1}$$

where $\tilde{p}(k_x, y, z)$ is the sound pressure amplitude in the 2D cross-section at position (y, z) and at wavenumber k_x in the x-direction. $\tilde{v}(k_x, y, z)$ is the normal velocity on the surface, ρ is the density of air, $\psi(k_x, y, z|y', z')$ is the Green's function and n is the direction normal to the surface Γ.

In Eq. (A1), the Green's function $\psi(k_x, y, z|y', z')$ takes the same form as the 2D fundamental solution

$$\psi(k_x, y, z|y', z') = -i\frac{1}{4}H_0^{(2)}(k_{2D}r) \tag{A2}$$

with $H_0^{(2)}(\cdot)$ being the Hankel function of the second kind and zero order, k_0 the wavenumber in air, and $k_{2D} = (k_0^2 - k_x^2)^{1/2}$.

The 2D boundary integral equation evaluated at a frequency ω_{2D} is

$$\tilde{p}(0, y', z') = -\int_{\Gamma}\left(i\rho\omega_{2D}\tilde{v}(0, y, z)\psi(0, y, z|y', z') + \tilde{p}(0, y, z)\frac{\partial\psi(0, y, z|y', z')}{\partial n}\right)d\Gamma \tag{A3}$$

Therefore, to obtain the solution at frequency ω and wavenumber k_x, the 2D solution should be evaluated at the equivalent frequency $\omega_{2D} = c_0 k_{2D}$, and the solution should be multiplied by the factor ω/ω_{2D} to recover Eq. (A1).

References

1   Commission Regulation (EU) No 1304/2014 of 26 November 2014 on the technical specification for interoperability relating to the subsystem 'rolling stock — noise' amending Decision 2008/232/EC and repealing Decision 2011/229/EU, Official Journal of the European Union L356 (12 December 2014) 421-437.

2   ISO 3095:2013, Acoustics – Railway applications – Measurements of noise emitted by railbound vehicles, International Organization for Standardization, Geneva, 2013.

3   Galijatovic E, Eichlseder M, Heindl SF, Klug C (2022) Integrity of virtual testing for crash protection. Front. Future Transp. 3:914489. https://doi.org/10.3389/ffutr.2022.914489

4   Huizinga FTMJM, Van Ostaijen RAA, Van Oosten Slingeland A (2002) A practical approach to virtual testing in automotive engineering. J Eng Des 13:33-47. https://doi.org/10.1080/09544820110090304

5   Dressler K, Speckert M, Bitsch G (2009) Virtual durability test rigs for automotive engineering. Vehicle Syst Dyn 47:387-401. https://doi.org/10.1080/00423110802056255

6   You SS, Fricke D (2011) Advances of virtual testing and hybrid simulation in automotive performance and durability evaluation. SAE Int J Mater Manuf 4:98-110. https://doi.org/10.4271/2011-01-0029

7   Bezin Y, Funfschilling C, Kraft S, Mazzola L (2015) Virtual testing environment tools for railway vehicle certification. Proc IMechE Part F: J Rail Rapid Transit 229:755-769. https://doi.org/10.1177/0954409715587596

8   Funfschilling C, Perrin G, Sebes M, Bezin Y, Mazzola L, Nguyen-Tajan ML (2015) Probabilistic simulation for the certification of railway vehicles. Proc IMechE Part F: J Rail Rapid Transit 229:770-781. https://doi.org/10.1177/0954409715589395

9   Grappein E, Rueter A (2015) Head pressure pulse in open air: Full assessment by computational fluid dynamics as a new standard. Proc IMechE Part F: J Rail Rapid Transit 229:570-580. https://doi.org/ 10.1177/0954409715585369

10   Sima M, Eichinger S, Blanco A, Ali I (2015) Computational fluid dynamics simulation of rail vehicles in crosswind: Application in norms and standards. Proc IMechE Part F: J Rail Rapid Transit 229:635-643. https://doi.org/10.1177/0954409714551013

11   Bruni S, Bucca G, Carnevale M, Collina A, Facchinetti A (2018) Pantograph–catenary interaction: recent achievements and future research challenges. Int J Rail Transp 6:57-82. https://doi.org/10.1080/23248378.2017.1400156

12   Bongini E, Cordero R (2015) Virtual testing within the TSI Noise: how to introduce numerical simulation into a certification process. In: J.C.O. Nielsen, et al. (Eds) Proceedings of 11th International Workshop on Railway Noise, Uddevalla, Sweden, 9-13 September 2013, Notes on Numerical Fluid Mechanics & Multidisciplinary Design 126:221-228. https://doi.org/10.1007/978-3-662-44832-8_29

13   Bongini E (2015) A virtual certification process (validated). EU FP7 project ACOUTRAIN, grant agreement no. 284877, Deliverable D1.8.

14   Frid A, Orrenius U, Kohrs T, Leth S (2012) BRAINS - the concepts behind a quick and efficient tool for prediction of exterior and interior railway vehicle noise. Proc Acoustics 2012, Nantes, France, April 2012.

15   Bistagnino A, Squicciarini G, Orrenius U, Bongini E, Sapena J, Thompson D (2015) Acoustical source modelling for rolling stock vehicles: the modeller's point of view. Proc Euronoise, Maastricht, June 2015.

16   Thompson D, Squicciarini G (2014) Basic global prediction tool and user manual (final update of D4.2). EU FP7 project ACOUTRAIN, grant agreement no. 284877, Deliverable D4.7.

17   ISO 9614-2 (1996) Determination of sound power levels of noise sources using sound intensity - Part 2: Measurement by scanning. International Organization for Standardization, Geneva.

18   ISO 3744 (2010) Acoustics - Determination of Sound Power Levels of Noise Sources Using Sound Pressure, International Organization for Standardization, Geneva.

19   Orrenius U, Betgen B, Feng L, Åbom M, Latorre Iglesias E, Thompson D, Brunström S (2014) Rail vehicle source assessment within a virtual certification process, Proc. ISMA, Leuven, September 2014.

20   Li H, Thompson D, Squicciarini G, Liu X, Rissmann M, Denia FD, Giner-Navarro J (2020) Using a 2.5D boundary element model to predict the sound distribution on train external surfaces due to rolling noise. J Sound Vib 486:115599. https://doi.org/10.1016/j.jsv.2020.115599

21   Pierce AD (1974) Diffraction of sound around corners and over wide barriers. J Acoust Soc Am 55:941-955. https://doi.org/10.1121/1.1914668

22   Attenborough K, Li KM, Horoshenkov K (2007) Predicting Outdoor Sound. CRC Press, London.

23   Haddon WJ, Pierce AD (1981) Sound diffraction around screens and wedges for arbitrary point source locations. J Acoust Soc Am 69:1266-1276. https://doi.org/10.1121/1.385809

24   Mielenz KD (1997) Computation of Fresnel Integrals. J. Res. National Inst Stand Technol 102:3.

25   Delany ME, Bazley EN (1970) Acoustical properties of fibrous absorbent materials. Appl Acoust 3:105-116. https://doi.org/10.1016/0003-682X(70)90031-9

26   Broadbent RA, Thompson DJ, Jones CJC (2009) The acoustic properties of railway ballast. Proc Euronoise 2009, Edinburgh.

27   Thompson D (2009) Railway noise and vibration: mechanisms, modelling and means of control. Elsevier, Oxford.

28   Fahy F, Thompson D (2015) Fundamentals of Sound and Vibration. CRC Press, Boca Raton.

29   Zhang X, Jeong H, Thompson D, Squicciarini G (2019) The noise radiated by ballasted and slab tracks. Appl Acoust 151:193-205. https://doi.org/10.1016/j.apacoust.2019.03.012

30   Bolin K, Rissmann M, Paillasseur S, Thompson DJ (2023) Measured source data for two selected sources based on sound intensity and on a 3D quantitative acoustic source imaging technique. Shift2Rail / H2020 project TRANSIT, grant agreement no. 881771, Deliverable D1.2.

31   Cierco E, Bolin K, Rissmann M, Thompson DJ, Zhao D (2023) Validation of source and transmission models on a rail vehicle at stand-still. Shift2Rail / H2020 project TRANSIT, grant agreement no. 881771, Deliverable D1.5.